Moisture sources and dynamics over southeastern Tibetan Plateau reflected in dual water vapor isotopes

Zhongyin Cai[1*], Rong Li[1], Cheng Wang[1], Qiukai Mao[1], Lide Tian[1]

[1]Institute of International Rivers and Eco-security, Yunnan Key Laboratory of International Rivers and Transboundary Eco-security, Ministry of Education Key Laboratory for Ecosecurity of Southwest China, Yunnan University, Kunming, China

*Corresponding author: Zhongyin Cai (czypil@gmail.com and z.cai@ynu.edu.cn)

Abstract

The Tibetan Plateau (TP) serves as a water tower for major rivers in Asia, and mountain valleys in southeastern TP are key channels for moisture entering the TP. Water resources on the TP are experiencing spatially opposite changes due to climate change, and understanding the sources and dynamics of atmospheric moisture is vital. To investigate the role of ocean surface evaporation, continental air mass intrusion, and rain-vapor interaction, we present a three-year daily time series of near-surface water vapor isotope compositions ($\delta^{18}O$ and d-excess) from the South-East TP station. We find that apparent negative correlations between d-excess and relative humidity over the Indian Ocean mainly reflect their similar seasonality. When analyzed for different seasons, the correlation is insignificant or only explains a marginal fraction of variance. Therefore, caution is required when interpreting the d-excess as a conservative tracer of ocean surface evaporation. Instead, local and upstream specific humidity is the

22   main factor determining non-monsoon season d-excess variability due to the intrusion of cold and dry air from upper

23   levels. During the summer monsoon season, d-excess and $\delta^{18}O$ mainly reflect the effect of raindrop evaporation on

24   humidity during transport which decreases lower vapor $\delta^{18}O$ but increases d-excess values. These findings provide

25   new insights into the significance of using water isotopes to track moisture sources and dynamics over the TP with

26   seasonally alternating circulation systems. Particularly, the findings for d-excess will improve the understanding of

27   different moisture sources and guide the interpretation of d-excess derived from other water bodies and ice cores.

1 Introduction

30   The Tibetan Plateau (TP) and its surrounding regions, also termed the Third Pole and the Asian Water Tower,

31   form the highest and largest plateau on Earth that influences climatic and hydrological systems at regional to global

32   scales, such as the formation of the Asian Summer Monsoon (Wu et al., 2022; Yao et al., 2022). In addition, the TP

33   stores the largest amount of frozen water outside of polar regions and sustains freshwater supplies of major river

34   systems in Asia. However, the water balance on the TP has experienced significant changes under the backdrop of

35   global warming (Yao et al., 2022). For instance, the southeastern TP is experiencing a drying trend while wetting in

36   the northern TP (Jiang et al., 2023; Zhang et al., 2023). Atmospheric water vapor is the input of the water storage

37   system and understanding its sources and dynamics is vital for understanding the imbalance of TP's hydrological

38   system.

39   Water stable isotopes are natural tracers of the water cycle (Bowen et al., 2019; Galewsky et al., 2016) and

40   have been intensively studied on the TP in precipitation, surface water, and ice cores (Yao et al., 2013; Thompson

41   et al., 2024; Bershaw, 2018). In general, precipitation isotope ratios ($\delta^{18}O$ and δ^2H) over the southern TP have lower

42   values during the summer monsoon season and higher values during the non-monsoon season under the influence

43 of the westerlies (He et al., 2015; Tian et al., 2007; Guo et al., 2024; Yang et al., 2017). Recent studies have

44 confirmed that monsoon convection at upstream along moisture transport pathways, rather than local precipitation

45 amount, is the key process that controls summer monsoon season precipitation $\delta^{18}O$ (Cai et al., 2017; He et al.,

46 2015). Different processes have been proposed to elucidate the relationship between precipitation $\delta^{18}O$ and

47 convection where the amount effect (Dansgaard, 1964) is present (Bowen et al., 2019; Galewsky et al., 2016). A

48 relatively classical interpretation is that the continuous rainout associated with stronger convection could cause

49 depleted precipitation following the Rayleigh distillation (Cai and Tian, 2016; Scholl et al., 2009; Vuille et al., 2003).

50 Another interpretation emphasized the role of rain-vapor interaction that partial evaporation of raindrops formed at

51 higher altitudes isotopically depletes lower tropospheric water vapor and then affects subsequent precipitation

52 isotope compositions (Risi et al., 2008a; Kurita et al., 2011; Cai et al., 2018; Lee and Fung, 2008). Observations of

53 vapor isotope compositions could help disentangle the different processes involved in the amount effect, especially

54 the secondary parameter deuterium excess (d-excess). The d-excess is defined as $\delta^2H - 8\delta^{18}O$ by Dansgaard (1964)

55 and mainly reflects the effects of kinetic fractionation. The rainout process mostly involves equilibrium fractionation

56 while raindrop evaporation is associated with kinetic fractionation, and they can therefore have different d-excess

57 signatures in water vapor. Isotopic compositions in the vapor phase have only been observed at a few stations on

58 the TP and isotope ratios (δ values) have been the major focus of previous studies (Tian et al., 2020; Dai et al., 2021;

59 Chen et al., 2024; Yu et al., 2016; Yu et al., 2015), less is known about vapor d-excess.

60   It is less certain regarding what caused higher isotope ratios during the non-monsoon season. Following the

61 regional amount effect (Galewsky et al., 2016; Bowen et al., 2019), high $\delta^{18}O$ values could be explained by

62 weakened convection during the non-monsoon season. However, precipitation $\delta^{18}O$ is lower during late- to post-

63 monsoon season in regions extending from the southeastern TP to the head of the Bay of Bengal (BOB), which is

64 not consistent with the weakening of convection (Breitenbach et al., 2010; Cai and Tian, 2020). Shifts of moisture

65 transport pathways between convection active and non-active regions have been invoked to explain this abnormal

66 seasonal pattern (Cai and Tian, 2020; Lekshmy et al., 2022). On the other hand, higher precipitation δ^{18}O

67 accompanied by higher d-excess during the non-monsoon season has been interpreted as more intense continental

68 recycling or moisture from the Mediterranean delivered by the westerlies compared with moisture from the Indian

69 Ocean during the summer monsoon (Tian et al., 2007; Yao et al., 2013; An et al., 2017; Breitenbach et al., 2010). In

70 addition, understanding of the atmospheric water cycle for a full seasonal cycle is complicated by the lack of

71 precipitation during the non-monsoon season which can be compensated by monitoring atmospheric water vapor

72 isotopes as it is not limited by precipitation events.

73   Both theoretical predictions and observations over ocean surface suggested that d-excess reflects ocean surface

74 evaporation conditions, such as sea surface temperature (SST) and relative humidity normalized to SST (RH$_{SST}$)

75 (Merlivat and Jouzel, 1979; Bonne et al., 2019; Liu et al., 2014; Craig and Gordon, 1965). Interpretations of d-

76 excess over the TP also frequently invoke these relationships with ocean evaporation conditions (Zhao et al., 2012;

77 Shao et al., 2021; Chen et al., 2024; Liu et al., 2024). However, relationships with either RH$_{SST}$ or SST are much

78 weaker than those observed over ocean surface. For instance, Shao et al. (2021) showed significant correlations

79 between an ice core d-excess record derived from the central TP and RH$_{SST}$ over the northern BOB and Arabian Sea

80 (AS). However, the correlation coefficient is only -0.44 and the slope between d-excess and RH$_{SST}$ is as steep as -

81 0.99‰ %$^{-1}$. The slope over oceanic regions generally ranges from -0.3‰ %$^{-1}$ to -0.6‰ %$^{-1}$ based on in-situ

82 observations (Bonne et al., 2019; Liu et al., 2014; Benetti et al., 2014; Uemura et al., 2008). Many studies have

83 suggested that d-excess at terrestrial sites is not a conservative tracer of evaporation conditions at the oceanic source

84 regions (Fiorella et al., 2018; Aemisegger et al., 2014; Welp et al., 2012; Wei and Lee, 2019; Samuels‐Crow et al.,

85 2014). Besides temporal variations, ice core d-excess values are generally higher than that observed in precipitation

86 at lower altitudes on the TP (Shao et al., 2021; Tian et al., 2001; Zhao et al., 2012; Joswiak et al., 2013; Zhao et al.,

87   2017; Thompson et al., 2000). It is still unclear what caused the abnormally high *d*-excess in these high-altitude ice

88   cores relative to precipitation and river isotope observations at lower altitudes.

89   Mountain valleys in the southeastern TP are believed to be major moisture transport channels delivering water

90   vapor toward the TP (Araguás-Araguás et al., 1998; Tian et al., 2007; Yao et al., 2013). Therefore, we started a water

91   vapor sampling campaign at the South-East Tibetan Plateau Station for integrated observation and research of alpine

92   environment (SETP) in June 2015 to study the moisture sources and dynamics and their influence on water isotope

93   compositions. Following the previous study (Yao et al., 2013), we define June-September (JJAS) as the summer

94   monsoon season. In contrast, we define November-April (Nov-Apr) as the non-monsoon season and May and

95   October as the transition between the two seasons. We will show distinct seasonal moisture sources and dynamics

96   between the two seasons as reflected in our vapor isotope observations and Lagrangian moisture source diagnostic.

97   Our results suggest that the apparent correlation between SETP vapor *d*-excess and oceanic surface evaporation

98   conditions is mainly a result of their similar seasonality. Alternatively, we suggest the intrusion of dry and cold air

99   by the westerlies from high altitudes contributes to high *d*-excess. In contrast, vapor δ^{18}O and *d*-excess confirm the

100   significant role of rain-vapor interaction in the amount effect during the summer monsoon season.

101   **2 Data and methods**

102   **2.1 Atmospheric water vapor sampling**

103   Atmospheric water vapor samples were collected using a cryogenic trapping method at the SETP station

104   (29°46'N, 94°44'E, 3326 m above sea level, and Fig. S1). The sampling system includes an air pump pumping

105   ambient air into the cold trap, a linked-ball-shaped glass cold trap, and an electric-powered system that creates and

106   maintains a cold environment filled by 95% ethanol as cold as below -80 °C. Ambient air was pumped from an inlet

107   at approximately 8 m above ground level through a Teflon tube to a glass trap immersed in a cold environment with

108   a temperature at -70 °C. The airflow rate was adjusted to ~5 L/min to allow 10-20 ml of water samples throughout

109   each sampling operation. During summers, the duration of each sampling operation is 24 hours. During dry winters,

110   however, we increased the sampling duration to 48 hours if a 24-hour sampling period cannot guarantee enough

111   sample amount. The samples were collected at 20:00 Beijing Standard Time (12:00 UTC). The efficiency of

112   extracting water vapor from ambient air was tested by connecting an additional cold trap to the outlet of the initial

113   cold trap, and no visible condensation was noticed in the additional cold trap (Yu et al., 2015). Further comparison

114   against direct measurements of vapor isotope composition by the Picarro L2130-i Cavity Ring Down Spectroscopy

115   (CRDS) at Lhasa, southern TP also confirmed the reliability of this method in sampling atmospheric water vapor

116   over the TP (Tian et al., 2020).

117   The sampling campaign was started on 25 June 2015 and ended on 14 June 2018. In total, 742 samples were

118   collected, and all the collected samples were kept frozen until transportation to the laboratory for measurements.

119   Samples collected before 28 June 2016 were measured at the Key Laboratory of Tibetan Plateau Earth System,

120   Environment and Resources, Institute of Tibetan Plateau Research, Chinese Academy of Sciences by a Picarro

121   L2130-i analyzer. Samples collected after 28 June 2016 were measured at the Institute of International River and

122   Eco-security, Yunnan University by a Picarro L2140-i analyzer. The isotopic values are calibrated and expressed

123   relative to Vienna Standard Mean Ocean Water 2 (VSMOW2). The precisions of measurements at both laboratories

124   are 0.1‰ for δ^{18}O, 0.4‰ for δ^2H, and 1.2‰ for d-excess.

125   **2.2 Meteorological data**

126   Daily local meteorological data before 2018, including precipitation amount, air temperature, air pressure, and

127   relative humidity, at the SETP station were provided by the station at the National Tibetan Plateau / Third Pole

128   Environment Data Center (Luo, 2018). Specific humidity (q) at SETP station is calculated from air temperature, air

129   pressure, and relative humidity at the station.

130   To facilitate analyses on larger spatial scales, we obtained meteorological variables (including 2-meter air

131   temperature, 2-meter dew point temperature, and SST, etc.) at 0.25°×0.25° and hourly resolution from the European

132   Centre for Medium-Range Weather Forecasts fifth generation reanalysis (ERA5) (Hersbach et al., 2019). RH_{SST} is

133   estimated from ERA5 2-meter meteorological data and SST using $RH_{SST} = e_{air}/e_{sat}$, where e_{air} is vapor pressure

134   of air and e_{sat} is saturation vapor pressure with respect to SST. We further obtained precipitation data at 0.1°×0.1°

135   and half-hourly resolution from the Integrated Multi-satellitE Retrievals for GPM (V07) (Huffman et al., 2023). In

136   addition, meteorological data at 1°×1° and 3-hourly resolution from the Global Data Assimilation System (GDAS)

137   are used to calculate air mass trajectories (see section 2.4).

138   **2.3 Theoretical framework for the understanding of isotope compositions and humidity**

139   Besides complex atmospheric circulation models, the evolution of vapor isotope compositions during different

140   moistening and dehydration processes can be understood by a compilation of atmospheric processes, such as

141   condensation, mixing, and raindrop evaporation, that lead to different pathways of isotopic evolution along

142   atmospheric humidity (Noone, 2012; Worden et al., 2007; Galewsky et al., 2016). The progressive condensation of

143   water vapor and removal as rain droplets or ice is best described by the canonical Rayleigh distillation model

144   (Dansgaard, 1964). In the Rayleigh distillation framework, condensate is removed from the air mass as soon as it

145   forms, and the isotope ratio of remaining vapor is described as $\delta = (1 + \delta_0)(q/q_0)^{\alpha-1} - 1$, where δ is the

146   isotope composition expressed as per mil deviation from a standard, q is the specific humidity, and α is the

147   fractionation factor. A subscript of 0 refers to the initial condition of the air mass. The falling raindrop may partially

148   evaporate or exchange isotopes with ambient vapor. As raindrops are formed at higher altitudes where water vapor

149   is depleted in heavy isotopes, the partial evaporation of raindrops would preferentially deplete its surrounding water

150   vapor but increase the atmospheric humidity, which leads to δ values lower than that predicted by the Rayleigh

151   distillation (Risi et al., 2008a; Worden et al., 2007). The evolution of δ along with q under partial evaporation of

152   raindrops can be described in a "super-Rayleigh" trajectory by inflating the effective fractionation factor (α_e) as

153    $\alpha_e = (1 + \phi)\alpha$, where ϕ quantifies the degree to which α deviates from equilibrium. We note that Worden et al.

154   (2007) and Noone (2012) have given different equations to quantify the deviations of α_e from α under different

155   degrees of raindrop evaporation, and the same deviation of α_e from α requires very different degrees of raindrop

156   evaporation. In this study, we follow the formulations by Noone (2012). Finally, the influence of air mass mixing

157   on humidity and isotopic compositions can be modeled through the mass balance perspective. When considering

158   mixing a dry air mass with a moist air mass, for instance, the specific humidity of mixed air mass can be described

159   as $q = f_{dry}q_{dry} + f_{moist}q_{moist}$, where f is the fraction of each air mass with the subscript denoting different air

160   masses and $f_{dry} + f_{moist} = 1$. Isotopic compositions of the mixed air mass can be derived similarly by solving the

161   mass balance equations for the light and heavy isotopes, respectively. The outcome of the mixing process leads to a

162   hyperbolic relationship between δ and q. In other words, $\delta \times q$ and q should have a linear relationship in the

163   mixing process (Fiorella et al., 2018). In a framework of the Keeling plots (Keeling, 1958), the intercept of the

164   regression between δ and $1/q$ or the slope between $\delta \times q$ and q gives an estimation of the isotope

165   composition of the moist end member.

166   Assuming a surface temperature of 25 °C and relative humidity of 85%, following the evaporation model by

167   Craig and Gordon (1965) we can derive that δ^{18}O of ocean surface evaporation is -11.5‰, δ^2H = -81.4‰, and d-

168   excess = 10.6‰. We use this isotopic signature of evaporated water vapor as a wet end member to model the

169   moistening process by mixing with ocean surface evaporation. A hypothetical dry end member from the Rayleigh

170   curve at q = 0.5 g/kg is chosen to represent the dehydrated dry air. The dehydration process by condensation is

171   modeled by choosing a starting point at the mixing line with a relative humidity of 80%. Similarly, the "super-

172   Rayleigh" distillation with partial rain evaporation is started from the same starting point. For the cases of "super-

173   Rayleigh", we simulated the isotopic evolution under two scenarios (Rain_evap_A and Rain_evap_B). Following

174   the equations in Noone (2012), Rain_evap_A represents that 2% of rain is evaporated and Rain_evap_B represents

175   an evaporated fraction of 5%. Mixing with evapotranspiration over south Asia and the TP is another way that could

176   modify the atmospheric humidity and vapor isotope compositions over southeastern TP. Accurate quantification of

177   the isotopic composition of land surface evapotranspiration is challenging. Given that the precipitation δ^{18}O over

178   south Asia is generally between -1.0‰ and -5.0‰ (Bowen and Wilkinson, 2002; Terzer-Wassmuth et al., 2021) and

179   transpiration may account two-thirds of evapotranspiration or more (Cao et al., 2022; Han et al., 2022; Good et al.,

180   2015), we assume the δ^{18}O of land surface evapotranspiration has a value of -5.0‰ as an upper bound. Similarly,

181   we assume that the *d*-excess of the wet end member of land surface evapotranspiration is 15.0‰.

182   **2.4 Air mass trajectory and moisture source diagnostic**

183   Air mass backward trajectories were calculated to investigate the air mass transport and diagnose moisture

184   sources and transport pathways toward SETP using the Hybrid Single-Particle Lagrangian Integrated Trajectory

185   model (HYSPLIT) (Stein et al., 2015). Trajectory calculation is driven by the meteorological data of the GDAS. We

186   released air parcels from 5 locations (the studied site and points displaced 0.2° in each cardinal direction) at 7

187   different vertical levels at 10, 50, 100, 200, 300, 400, and 500 m above ground level. For each day during the

188   sampling campaign, trajectories were initiated every 3 hours to calculate 10-day backward trajectories. In this setting,

189   280 trajectories were derived for each single day. Geographical and meteorological variables, including location,

190   pressure, temperature, specific humidity, rainfall amount, boundary layer height, and the terrain height along

191   trajectories, were stored at hourly intervals.

192   Moisture contribution along air mass trajectories to the humidity at SETP is quantified using the Lagrangian

193   moisture source diagnostic method of Sodemann et al. (2008). The method considers mass balance along the

194   trajectory and assigns increases in specific humidity (forward in time) as moisture uptake, and decreases in specific

195   humidity as moisture lost due to precipitation. The method also proportionally considers the decreased contribution

196   of early uptake due to the precipitation en route. We have previously adapted this method to quantify the moisture

197   sources of precipitation in sub-regions of South Asia and East Asia (Cai et al., 2018; Cai and Tian, 2020). The

198   diagnostic results suggest that the unattributed fraction of moisture arriving at SETP is ~5%, and therefore 10-day

199   trajectories are capable of diagnosing most of the moisture sources. Instead of focusing on quantifying the

200   evaporative moisture source from the Earth surface, in this study, we focus on the contribution of the air parcel itself

201   to the humidity at SETP. This variable is readily available from the diagnostic method, and the change of air parcel

202   contributions between time steps within the boundary layer is the moisture uptake from the Earth surface. The

203   moisture contribution by air parcel to humidity at SETP gives a measure of the importance of upstream air masses.

204   Using this variable as the weight, mean upstream geographical and meteorological variables are hence calculated

205   as weighted means. We also applied cluster analysis on the trajectories to visualize the major transport pathways

206   using the K-means clustering method. When calculating the mean trajectory for each cluster and meteorological

207   variables along each mean trajectory, the moisture contribution by air parcel is also considered as the weight to

208   calculate weighted means.

209   **3 Results**

210   **3.1 General characteristics**

211   In general, water vapor δ^{18}O values are at a lower level during the summer monsoon season and a higher level

212   during the non-monsoon season (Fig. 1a). Mean vapor δ^{18}O values are -18.4‰ for the non-monsoon season, -23.3‰

213   for the summer monsoon season, -16.9‰ for May, and -22.8‰ for October. During the onset of the summer

214   monsoon, the vapor δ^{18}O shows a dramatic decrease to lower values. Without a sharp rebound to values before the

215   summer monsoon, the δ^{18}O value shows a gradual increase trend from the end of the summer monsoon season

216   toward the highest values during spring and early summer. Although this region is significantly influenced by the

217   amount effect, the seasonal trend of vapor $\delta^{18}O$ does not strictly follow the seasonal variation of local precipitation.

218   For instance, local precipitation shows clear cessation after the summer monsoon (Fig. 1e) while $\delta^{18}O$ does not

219   rebound to the level before summer monsoon onset. These seasonal characteristics of vapor $\delta^{18}O$ is consistent with

220   precipitation $\delta^{18}O$ observed in southeastern TP, northeast India, and Bangladesh (Yao et al., 2013; Cai and Tian,

221   2020; Yang et al., 2017). Overall, water vapor d-excess also has lower values during the summer monsoon season

222   and higher values during the non-monsoon season (Fig. 1b). Mean vapor d-excess values are 18.3‰ for the non-

223   monsoon season, 11.9‰ for the summer monsoon season, 13.7‰ for May, and 14.9‰ for October. However, the

224   timing of the seasonal transition of vapor d-excess is different from that of vapor $\delta^{18}O$. The highest vapor d-excess

225   values generally occur during winter months when the air temperature and relative humidity (RH) are the lowest

226   (Fig. 1c and 1d) and the d-excess starts to decrease from spring which is earlier than the sharp drop of vapor $\delta^{18}O$

227   during the onset of the summer monsoon.
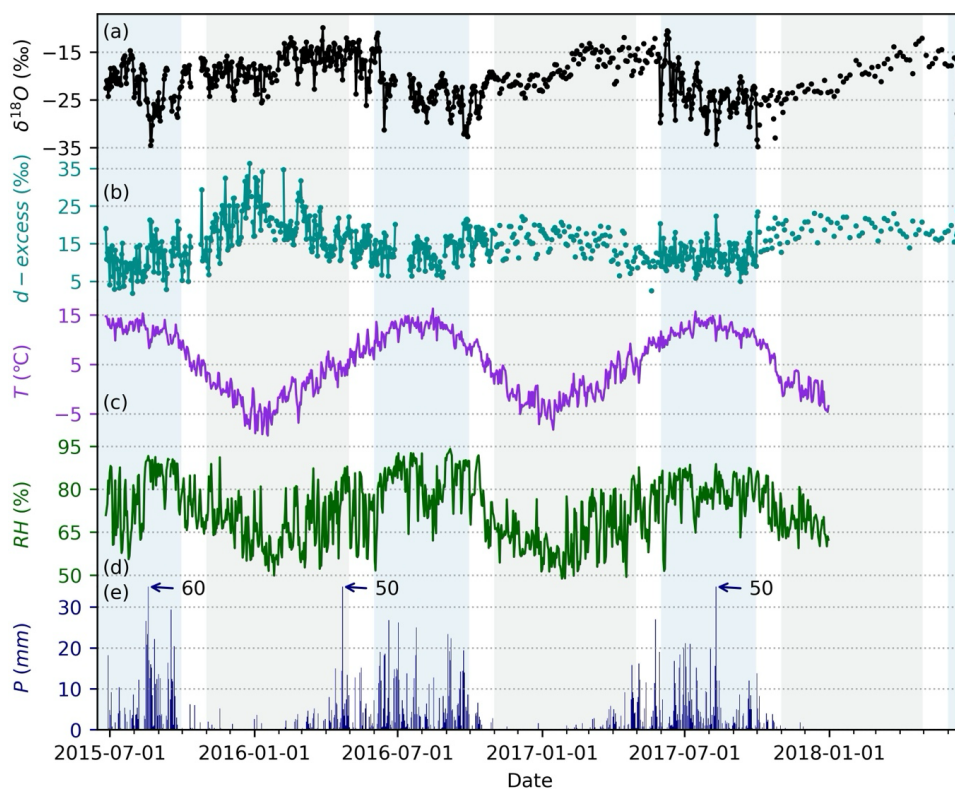
Figure 1. The general temporal variability of observed water vapor isotope compositions and daily local meteorological variables from 2015-2018: (a) $\delta^{18}O$, (b) *d*-excess, (c) air temperature, (d) relative humidity (RH), and (e) precipitation amount. The light blue shading highlights the summer monsoon season and the light steel blue shading highlights the non-monsoon season.

The linear relationship between paired $\delta^{18}O$ and δ^2H data points and their locations relative to the global meteoric water line (GMWL, $\delta^2H = 8\delta^{18}O + 10$) (Craig, 1961) generally provide additional insights into isotopic fractionation (Putman et al., 2019). The local meteoric water line (LMWL) estimated from all vapor δ^2H and $\delta^{18}O$ data points is $\delta^2H = 7.96\delta^{18}O + 14.04$ ($R^2 = 0.98$) which plots above but approximately parallel with the GMWL. This relatively higher intercept of vapor LMWL reflects the continental location of the site and further kinetic fractionation after ocean surface evaporation. The δ^2H-$\delta^{18}O$ relationship also varied seasonally. The vapor LMWL

239   for non-monsoon season is $\delta^2H = 7.58\delta^{18}O + 10.61$ ($R^2 = 0.96$) and for summer monsoon season is $\delta^2H = 7.53\delta^{18}O$

240    $+ 0.91$ ($R^2 = 0.99$). Non-monsoon season vapor isotope compositions mainly plot above the GMWL and even above

241   the overall vapor LMWL. While the majority of monsoon season isotope data plot below the overall vapor LMWL,

242   those data points that have the lowest δ values plot above the overall vapor LMWL indicating further kinetic

243   fractionation such as rain evaporation. Vapor isotope compositions for May are more similar to those during the

244   non-monsoon season but plot closer to the GMWL and LMWL, while data for October show a more similar behavior

245   with the monsoon season observations.
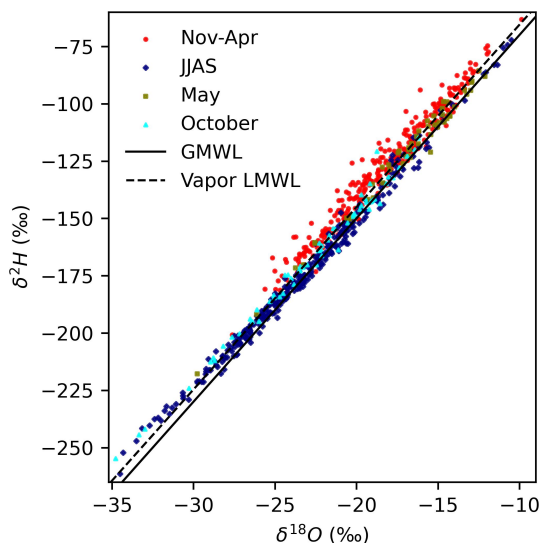
246

247   **Figure 2. Relationship between vapor δ^2H and $\delta^{18}O$. Data during the non-monsoon season (Nov-Apr),**

248   **the summer monsoon season (JJAS), May, and October are shown as red dots, navy diamonds, olive squares,**

249   **and cyan trangles, respectively. The solid line indicates the global meteoric water line (GMWL). The dashed**

250   **line indicates the local meteoric water line (LMWL) estimated from all vapor δ^2H and $\delta^{18}O$ data points.**

251   The relationships between vapor $\delta^{18}O$ and specific humidity (q) further indicate seasonally contrasting

252   moisture dynamics (Fig. 3a). Note that only data before 2018 are shown as local meteorological data are unavailable

253   in 2018. In addition, the sampling frequency during 2018 was reduced (Fig. 1) due to logistic issues. Therefore,

254   when analyzing relationships between vapor isotope compositions (δ^{18}O and d-excess) and meteorological variables

255   (both locally and regionally) we only focused on data before 2018. For months during the non-monsoon season, the

256   majority of data points fall above the Rayleigh distillation line but below the mixing line of an upper bound of

257   hypothetical evapotranspiration over South Asia, especially for the winter months. In contrast, data for the summer

258   monsoon season months predominately fall below the Rayleigh distillation line and are constrained by "super-

259   Rayleigh" lines with different degrees of rain evaporation. The relationships between $\delta \times q$ and q further indicate

260   seasonal contrast moisture source signatures (Fig. S3). Distribution of non-monsoon season $\delta \times q$ and q suggests

261   the mixing between a dry end member that has almost totally dehydrated through condensation and a moist end

262   member of surface evaporation or moisture that has been partially dehydrated through Rayleigh distillation (Fig.

263   S3). A simple estimation through the linear regression between $\delta \times q$ and q suggests δ^{18}O of the moist end

264   member for the non-monsoon season is -13.9‰ ± 0.6‰. The amount weighted annual mean precipitation δ^{18}O at

265   this site was about -14.5‰ (Yao et al., 2013). However, the overall estimation for the summer monsoon season

266   suggests δ^{18}O of the moist end member is -30.9‰ ± 1.8‰ which is much lower than the estimation for the non-

267   monsoon season. This exceptionally low value requires an additonal moisture source of rain evaporation that is

268   much depleted in heavy isotopes than surface evapotranspiration and is consistent with the distribution of δ^{18}O-q

269   below the Rayleigh distillation line (Fig. 3a).

270   The relationships between vapor d-excess and q also suggest seasonal contrasts in moisture dynamics (Fig. 3b).

271   During non-monsoon season months, vapor d-excess shows a negative correlation with q, and the highest d-excess

272   values are generally associated with the driest and coldest air (Figs. 1 and 3b). However, vapor d-excess does not

273   show a clear relationship with q and shows a substantial variability (~20‰ in range) at a given q during the summer

274   monsoon season. These relationships suggest that vapor d-excess is less predictable by q than δ^{18}O, except for low

275   humidity levels.
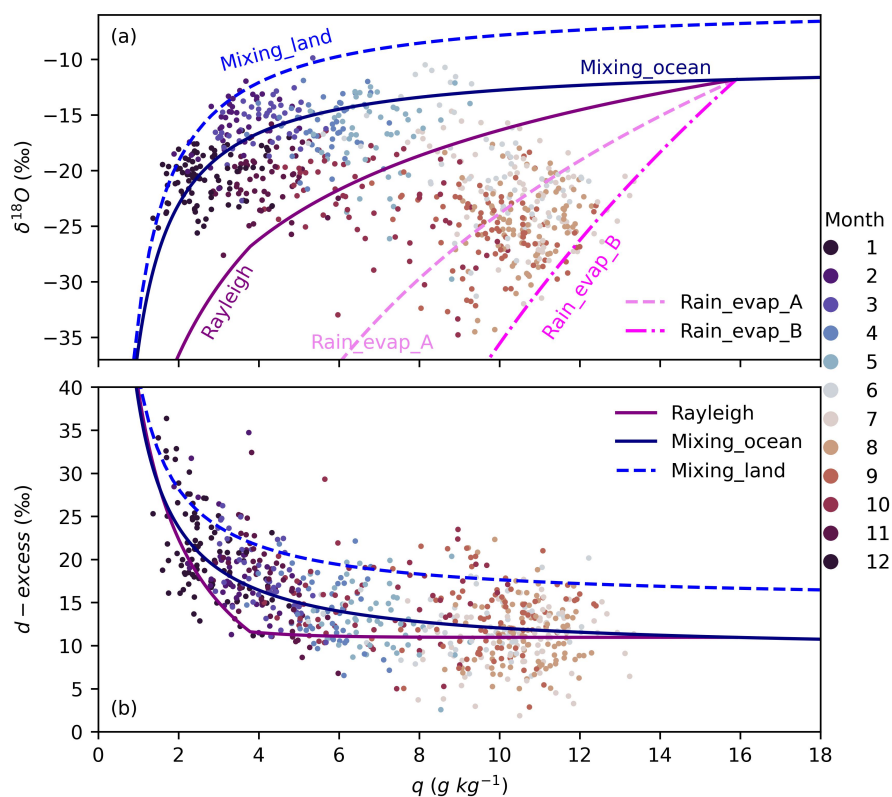
Figure 3. Relationships between vapor isotope compositions and specific humidity (q) from 2015-2017.

(a) scatter plot of $\delta^{18}O$ against specific humidity (q). (b) scatter plot of d-excess against q. The months for the

data points are color-coded. The reference lines are the same as those in Fig. S2, and interpretations of these

reference lines are referred to Fig. S2 and section 2.3.

3.2 Moisture sources and transport pathways for different seasons

To understand drivers of the seasonal contrasting moisture dynamics reflected in vapor isotope compositions,

we first analyzed the moisture sources and transport pathways during different seasons (Fig. 4). Note again that we

focus on the contribution by historical (last 10 days) air mass to humidity at SETP instead of moisture uptake from

the Earth surface. During the non-monsoon season, moisture is mainly transported by two branches with one from

the west of SETP by the westerlies (clusters Nov-Apr2 and Nov-Apr3) and the other from the south of SETP such

287   as the BOB (cluster Nov-Apr1). Quantitatively, the fraction of moisture from the south pathway and the sum of the

288   two west branches is comparable (52.4% vs. 47.7%). We note that if moisture contributions by air parcels are not

289   considered, trajectories for all three clusters are from the west of SETP and they only reflect the transport of air

290   masses (Fig. S4). These differences between pure air mass trajectories and considering moisture contribution by air

291   masses call for caution when interpreting air mass trajectories. During the summer monsoon season, moisture is

292   predominantly transported from the south of SETP by the summer monsoon. The moisture sources and transport

293   pathways for May show some similarities with the results for the non-monsoon season. Compared with the second

294   transport pathway during the non-monsoon (cluster Nov-Apr2), the second transport pathway during May (cluster

295   May2) shows an overall southward shift toward the AS. Although the air mass transport pattern during October is

296   also similar to that during the non-monsoon, the moisture sources and transport pathways for October show

297   similarities with the results for the summer monsoon season with a slight eastward shift (Figs. 4d and S4d).

298   Another emerging feature of moisture source distributions is that humidity at SETP is predominantly

299   contributed by air masses over proximal terrestrial regions, especially those regions in its south (Fig. 4). In contrast,

300   air masses over oceanic regions make a much smaller contribution to humidity at SETP. For instance, the 1% contour

301   of moisture contribution by air parcels over each 1°×1° grid box does not reach oceanic regions during all four

302   seasons. Therefore, moisture uptake of surface evaporation from oceanic regions, such as from the BOB and AS, is

303   also very limited as most of the moisture in air masses over these oceanic regions is lost by precipitation and

304   replenished by evapotranspiration during the transport toward SETP. This result questions whether vapor isotopic

305   compositions at SETP still preserve the meteorological information at the ocean surface.
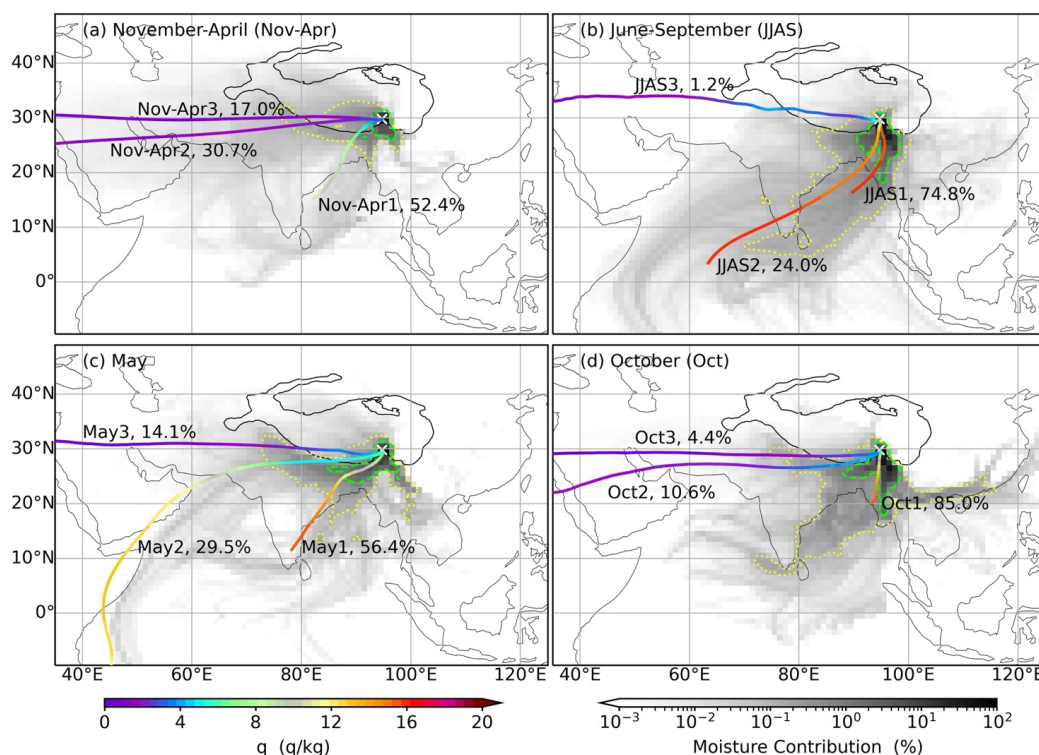
Figure 4. Moisture sources and transport pathways during different seasons from 2015-2017. (a) spatial distribution of relative contribution of moisture by all air parcels overall each 1°×1° box (shading) to humidity at the SETP station and specific humidity (*q*) along mean trajectories (weighted by the moisture contribution of air parcels) for the non-monsoon season of November-April (Nov-Apr). (b-d) are the same as (a), but for the monsoon season of June-September (JJAS, b), May (c), and October (d), respectivley. The dotted yellow and dashed green contours indicate the moisture contribution at 0.1% and 1%, respectively. The yellow crosses indicate the location of the SETP station. The black solid lines denote the Tibetan Plateau with altitude contour at 3000 m.

4 Discussion

4.1 Role of ocean surface evaporation conditions

Relationships between vapor d-excess and ocean surface evaporation conditions of RH_{SST} and SST are first

tested using all the data from 2015-2017 (Fig. 5a and Fig. S5a). Results indeed show negative correlations between

vapor d-excess and RH_{SST} over northern Indian Ocean, especially the northern part of AS and BOB (Fig. 5a).

Quantitively, slopes of the regression between d-excess and RH_{SST} over the northern Indian Ocean range from higher

than -0.1‰ %$^{-1}$ to values below -0.6‰ %$^{-1}$. The regression slopes over the northern BOB (10-22°N and 80-99°E)

and the eastern AS (7-20°N and 65-78°E; Fig. 5a) fall within the range reported in previous studies (Uemura et al.,

2008; Benetti et al., 2014; Liu et al., 2014; Bonne et al., 2019). Vapor d-excess and regional average RH_{SST} yields

an overall slope of -0.49‰ %$^{-1}$ (r = -0.52 and p < 0.01) for the eastern AS (Fig. S6) and -0.52‰ %$^{-1}$ (r = -0.55 and

p < 0.01) for the northern BOB (Fig. S7). However, the distribution of data in the d-excess and RH_{SST} space suggests

a clustering of data that observations during summer months are mainly located in the lower right with high RH_{SST}

and low d-excess, but in the upper left part of the space for winter months. During each season, there is substantial

variability in vapor d-excess for a given RH_{SST}. These results suggest that the apparent negative correlation between

d-excess and RH_{SST} may mainly arise from their opposite seasonality. Similarly, apparent negative correlations

between vapor d-excess and SST also emerge over the northern Indian Ocean (Fig. S5a). However, both theoretical

prediction (Merlivat and Jouzel, 1979) and in-situ observations above the ocean surface (Bonne et al., 2019; Liu et

al., 2014) suggest a positive correlation between vapor d-excess and SST. Therefore, we argue that the overall

correlations between SETP vapor d-excess and surface evaporation conditions over the northern Indian Ocean are

mainly a result of their seasonality and do not hold realistic causal relationships.

We further examined the relationship between vapor d-excess and RH_{SST} for the summer monsoon and non-

monsoon seasons, respectively. The negative correlation between vapor d-excess and RH_{SST} almost totally

337   diminishes, especially during the summer monsoon season when absolute values of correlation coefficients drop to

338   below 0.3 (Fig. 5b). Stronger correlations during the non-monsoon season (Fig. 5c) could be due to the overall

339   intraseasonal variation that d-excess is the highest during winter and lower at the beginning and ending stages (Fig.

340   1b) which could be accompanied with an opposite RH_{SST} trend. Even so, the correlations during the non-monsoon

341   still only explain a marginal fraction of variance in d-excess (10%-16% at maximum over the northern BOB).

342   Similarly, correlations with SST over the northern Indian Ocean also become trivial when separately considering

343   the summer monsoon or non-monsoon season (Fig. S5). In summary, vapor d-excess at SETP is less likely a

344   conservative tracer of surface evaporation conditions (neither RH_{SST} nor SST) over the northern Indian Ocean.

345   Therefore, it should be cautious when interpreting d-excess in meteoric water or paleo archives from the TP as a

346   proxy of evaporation conditions over the Indian Ocean.
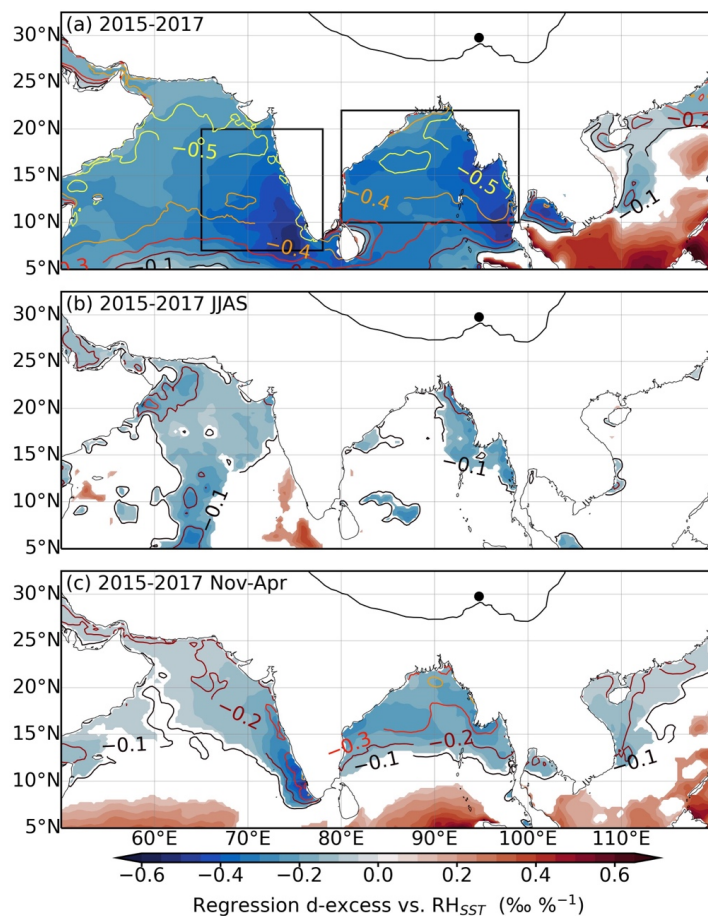
Figure 5. Relationships between water vapor *d*-excess and relative humidity scaled to sea surface temperature (RH$_{SST}$). (a) regression of vapor *d*-excess against RH$_{SST}$ (shading and only values significant at the 95% significance level are shown) and correlation coefficients between them (contours at an interval of 0.1 and only negative correlations are shown) for all the data from 2015-2017. (b) and (c) are the same as (a) but only for the data within the summer monsoon season (JJAS) or the non-monsoon season (Nov-Apr), respectively. The black dots indicate the location of the SETP station. The black solid lines denote the Tibetan Plateau with altitude contour at 3000 m.

4.2 Role of dry and cold air intrusion during the non-monsoon season

355

356   Both theoretical predictions by the Rayleigh model and observations during the non-monsoon season suggest

357   an increasing trend of vapor d-excess when q goes to extremely low values (Fig. 2). In addition, results for both air

358   mass transport and moisture transport show the dominant role of the westerlies (Figs. S4a and 4a). Therefore, we

359   hypothesize that the mixing of cold and dry air transported by the westerlies from higher altitudes with surface vapor

360   controls vapor isotope compositions during the non-monsoon season. Surface vapor influenced by recycled moisture

361   from terrestrial evapotranspiration would further elevate vapor d-excess at a given q (Fig. 3b). We first did a

362   composite analysis on moisture sources and transport pathways for the highest (higher than 30‰ and n = 10) and

363   lowest d-excess observations (lower than 10‰ and n = 8) during the non-monsoon season (Fig. 6). For high vapor

364   d-excess values, moisture is predominantly transported by westerlies from the west of SETP, such as over the TP

365   and northwestern India. In addition, air masses along backward trajectories are characterized by extremely low q

366   i.e. as low as below 2 g kg^{-1} along the mean trajectories (weighted by the moisture contribution) over the TP (Fig.

367   6a). For low d-excess cases, a substantial amount of moisture transport pathways (account for 39.2% by the L1

368   cluster, Fig. 6b) shift toward more humid areas of northeast India, Bangladesh, and the BOB. This contrasting

369   moisture transport pattern between high and low d-excess cases agrees with our hypothesis that the high d-excess

370   is associated with dry and cold air transported by the westerlies.
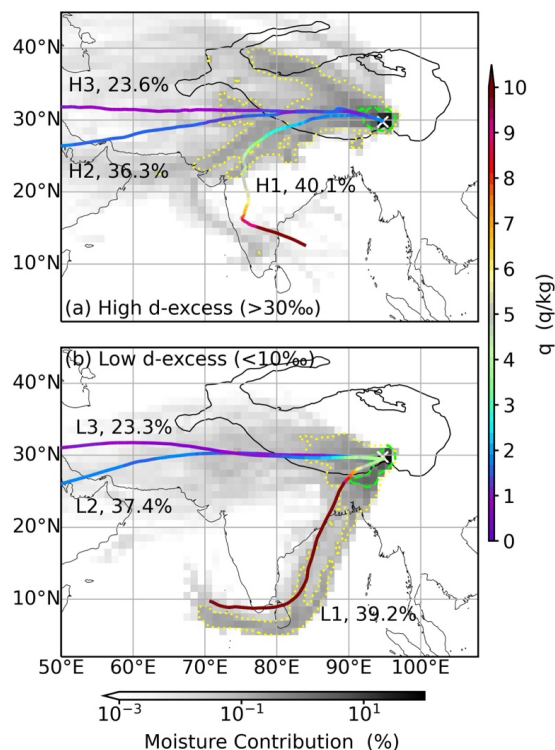
Figure 6. Composite of moisture sources and transport pathways for high and low *d*-excess days during the non-monsoon season of November-April. (a) spatial distribution of relative contribution of moisture by all air parcels overall each 1°×1° box (shading) to humidity at the SETP station and specific humidity (*q*) along mean trajectories (weighted by the moisture contribution of air parcels) for *d*-excess values higher than 30‰ during the non-monsoon season (n = 10). (b) is the same as (a) but for *d*-excess lower than 10‰ (n = 8). The yellow crosses indicate the location of the SETP station. The black solid lines denote the Tibetan Plateau with altitude contour at 3000 m.

The relationship between vapor *d*-excess and the intrusion of cold and dry air is further tested by relationships among vapor *d*-excess, local *q*, upstream *q*, upstream air temperature, and upstream air altitude (Fig. 7). Upstream variables are mean values along the 10-day backward trajectory weighted by the moisture contribution of the air parcel at each time step (section 2.4). The non-monsoon season vapor *d*-excess shows robust negative correlations

383   with q both at the local scale as well as at upstream ($r = -0.65$ and -0.67, respectively, and $p < 0.01$ for both). At the

384   same time, low q is associated with air masses with low temperature and from high altitudes (Figs. 7c and 7d). This

385   effect could also have an impact on vapor $\delta^{18}O$. $\delta^{18}O$ during the high d-excess cases is lower than $\delta^{18}O$ during the

386   low d-excess cases (at a significance level of 95.3%), and the overall correlation coefficient between $\delta^{18}O$ and d-

387   excess during the non-monsoon season is -0.29 ($p < 0.01$). Correlations between $\delta^{18}O$ and local q ($r = 0.42$ and $p <$

388   0.01) or upstream q ($r = 0.38$ and $p < 0.01$) are weaker than the correlations between d-excess and q. The relationship

389   between non-monsoon season $\delta^{18}O$ and humidity is mainly expressed as the relationship between $\delta \times q$ and q (r

390   $= 0.82$ for local q and $r = 0.90$ for upstream q).

391   We further analyzed the spatial distribution of correlations between SETP vapor isotope compositions ($\delta^{18}O$

392   and d-excess) and 2-meter air temperature as well as humidity measured by 2-meter dew point temperature during

393   the non-monsoon season (Fig. 8). Results show significant negative correlations between d-excess and dew point

394   temperature at the regional scale over southeastern TP, northeast India, and northern Bangladesh (Fig. 8a).

395   Correlations with air temperature are generally similar with correlations between d-excess and dew point

396   temperature but the most significant correlations are in a smaller region (Fig. 8b). In contrast, correlations between

397   $\delta^{18}O$ and dew point temperature is not as strong as that for d-excess (Fig. 8c). Instead, $\delta^{18}O$ shows stronger positive

398   correlations with air temperature over the India subcontinent and the northwestern part of southeast Asia (Fig. 8d).

399   Extremely high d-excess values at very low q levels are predicted in Fig. 3b, and previous study has shown

400   that as q approaches zero, vapor d-excess can approach 7000‰ following the Rayleigh distillation trajectory (Bony

401   et al., 2008) caused by the definition of the d-excess (Dütsch et al., 2017). High vapor d-excess values have also

402   been observed in low humidity conditions such as in the polar regions (Bonne et al., 2014; Steen-Larsen et al., 2017)

403   or at high altitudes (Samuels‐Crow et al., 2014; Webster and Heymsfield, 2003; Sayres et al., 2010; Sodemann et

404   al., 2017). Therefore, we infer that the increasing trend of vapor d-excess along with decreasing local q, upstream

405 *q,* and regional dew point temperature is a result of intensified mixing with dry and cold subsiding air transported

406 by the westerlies from high altitudes. Relationships between upstream *q* and upstream air temperature as well as

407 altitude support this inference that low humidity condition is associated with subsiding dry and cold air from high

408 altitudes (Figs. 7c and 7d). Therefore, vapor *d*-excess during the non-monsoon not only provides information on the

409 specific humidity but also indicates the source of humidity.
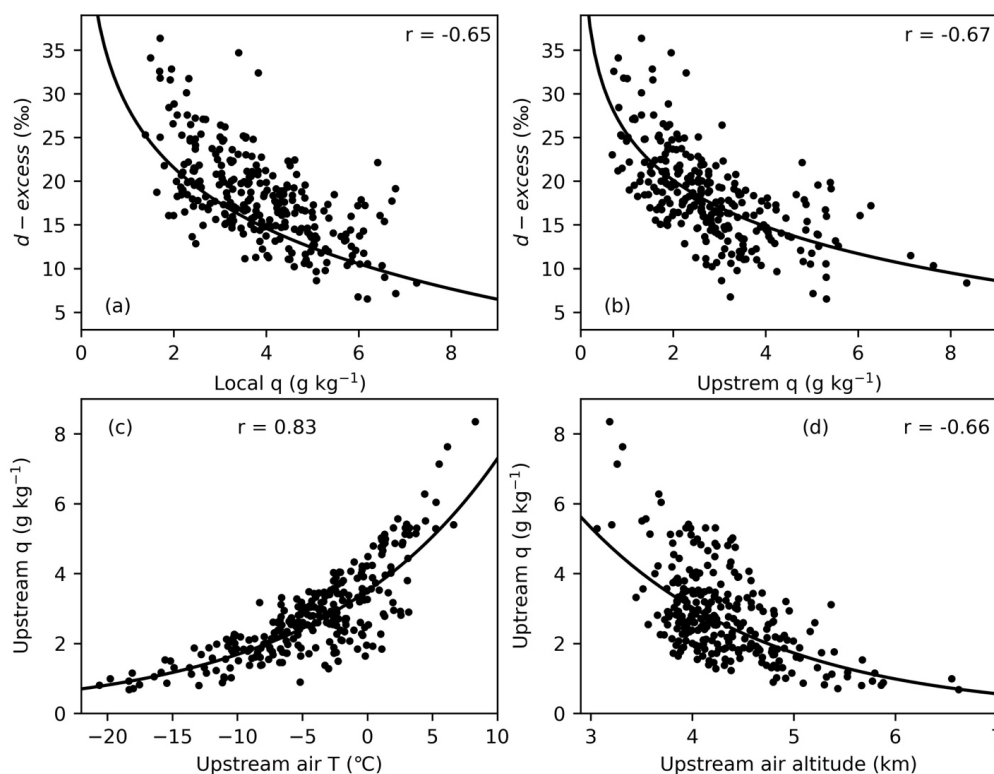
410

411 **Figure 7. Relationships among water vapor *d*-excess, local specific humidity (*q*), upstream *q*, upstream**

412 **air temperature (T), and upstream air altitude during the non-monsoon season of November-April. (a) scatter**

413 **plot of *d*-excess against local *q*. (b) scatter plot of *d*-excess against upstream weighted-mean *q*. (c) scatter plot**

414 **of upstream *q* against upstream air T. (d) scatter plot of upstream *q* against upstream air altitude. All the**

415 **upstream variables are mean values along backward trajectories weighted by the moisture contribution of**

416 **air parcels. The solid curves indicate the log regression between the respective variables with the correlation**

417 **coefficients indicated by the numbers.**
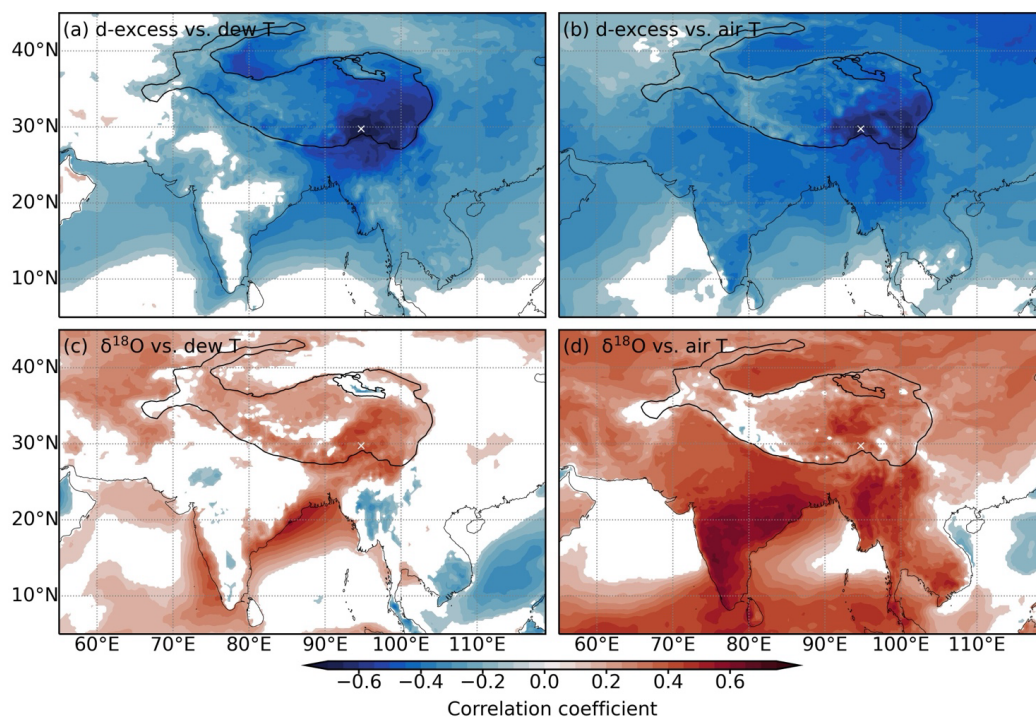
419 **Figure 8. Spatial distribution of correlation coefficients among water vapor isotope compositions, dew**

420 **point temperature, and air temperature during the non-monsoon season of November-April. (a) spatial**

421 **distribution of correlation coefficients between SETP vapor *d*-excess and 2-meter dew point temperature. (b)**

422 **the same as (a) but with 2-meter air temperature. (c) the same as (a) but between δ^{18}O and 2-meter dew point**

423 **temperature. (d) the same as (c) but with 2-meter air temperature. Only values significant at the 95%**

424 **significance level are shown. The white crosses indicate the location of the SETP station. The black solid lines**

425 **denote the Tibetan Plateau with altitude contour at 3000 m.**

426 **4.3 Role of rain-vapor interaction during the summer monsoon season**

427   Different from the significant dependence of vapor *d*-excess on specific humidity during the non-monsoon

428 season, vapor *d*-excess is not correlated with specific humidity (r = 0.04 and p = 0.51) during the summer monsoon

429   season. The behavior of δ^{18}O is also distinct during the two seasons (Fig. 3). Distribution of summer monsoon

430   season observations in the δ^{18}O-q space suggests that the vapor has undergone a certain degree of rain-vapor

431   interaction by rain evaporation (Fig. 3a). On the other hand, partial rain evaporation in an unsaturated atmospheric

432   environment is associated with kinetic fractionation which decreases the d-excess values of the raindrop but

433   increases the d-excess of surrounding vapor (Risi et al., 2008b). This effect of rain-vapor interaction on vapor isotope

434   compositions has been suggested as a major process responsible for the amount effect in the tropics (Risi et al.,

435   2008a; Kurita et al., 2011; Bowen et al., 2019; Galewsky et al., 2016). Therefore, we hypothesize that vapor isotope

436   compositions during the summer monsoon season at SETP are controlled by the degree of rain-vapor interaction.

437   The first evidence supporting this hypothesis is that vapor δ^{18}O is significantly correlated with d-excess during the

438   summer monsoon season (r = -0.55 and p < 0.01, Fig. 9a). In addition, there is a trend that vapor δ^{18}O and d-excess

439   are less correlated when δ^{18}O is high and the opposite for low δ^{18}O levels (Figs. 9a and S8). If there is no rain, rain-

440   vapor interaction is not possible. Therefore, we flitted data during days when the daily precipitation amount is not

441   less than 2 mm as rainy days and days with precipitation less than 2 mm as no rain occurs locally (non-rainy days).

442   Vapor δ^{18}O during rainy days is significantly higher than during non-rainy days and the opposite trend applies for

443   d-excess (p < 0.01 for both δ^{18}O and d-excess) (Figs. 9b and 9c). The correlation between vapor δ^{18}O and d-excess

444   during rainy days becomes stronger (r = -0.69 and p < 0.01). However, vapor δ^{18}O is still negatively correlated with

445   d-excess during non-rainy days (r = -0.40 and p < 0.01). Even if a stricter threshold of 0 mm for daily precipitation

446   amount is used for flittering non-rainy days, there is still a significant negative correlation between vapor δ^{18}O and

447   d-excess (r = -0.37 and p < 0.01). In addition, correlations with local precipitation amount are weak both for δ^{18}O

448   (r = -0.31 and p < 0.01) and d-excess (r = 0.26 and p < 0.01). Therefore, we further infer that the effect of rain-vapor

449   interaction is not only from the local scale but also inherits the history of rain-vapor interaction before vapor has

450   been transported to SETP.

451
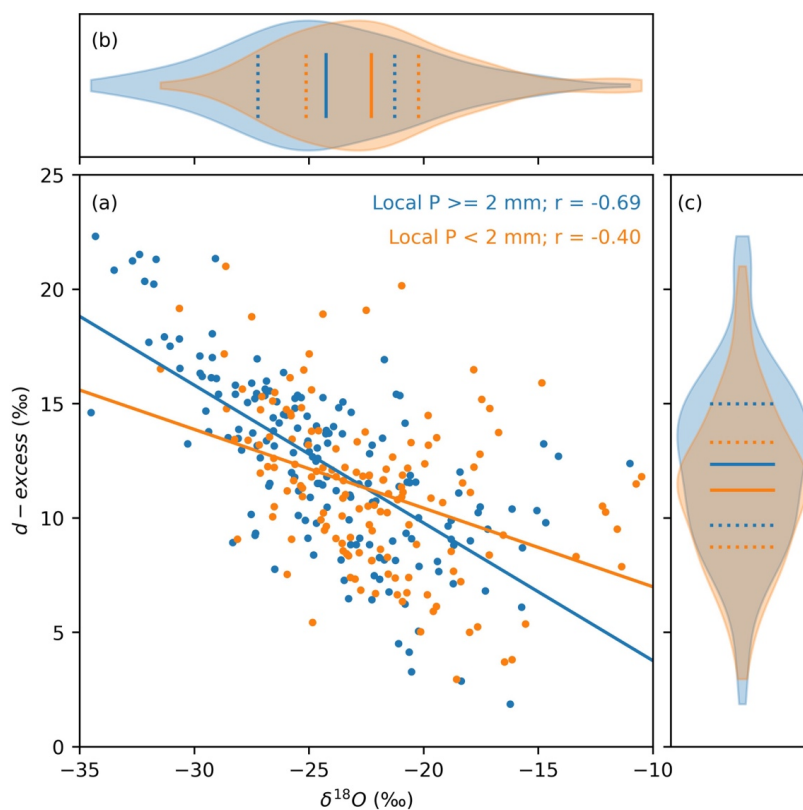
Figure 9. Relationships between SETP vapor *d*-excess and δ¹⁸O during the summer monsoon season. (a)

scatter plot of *d*-excess against δ¹⁸O and linear regression lines between them. (b) distribution of δ¹⁸O values

with the dashed lines indicate values at the lower and upper quartiles and the solid lines indicate the mean

values. (c) is the same as (b) but for *d*-excess. Orange colors indicate data observed during daily precipitation

amount less than 2 mm and blue colors indicate data observed during days with precipitation amount not

less than 2 mm.

If there is a larger amount of rainfall, the effect of rain-vapor interaction on atmospheric humidity would be

stronger. Therefore, we use total precipitation amount (P_{acc}) as a measure of rain-vapor interaction. To account for

the history during moisture transport, the total precipitation amount during several days before sampling is

considered. We have tested the relationships between vapor isotope compositions (δ¹⁸O and *d*-excess) and P_{acc} over

462   1-10 days prior to sampling (Figs. S9 and S10). Vapor d-excess reaches an optimal correlation with P_{acc} when the

463   total precipitation amount during 3 days before sampling (P_{acc_3d}) is considered. Vapor $\delta^{18}O$ shows a slightly longer

464   memory and reaches an optimal correlation with P_{acc} when the total precipitation amount during 5-6 days before

465   sampling is considered. Fig. 10 shows the spatial distribution of correlations between vapor isotope compositions

466   ($\delta^{18}O$ and d-excess) and P_{acc_3d}. Vapor d-excess shows significant positive correlations with P_{acc_3d} in the region

467   surrounding SETP with a spatial scale of ~5°×5° and the positive correlation extends southwestward to the foothill

468   of the Himalayas (Fig. 10a). In contrast, vapor $\delta^{18}O$ shows significant negative correlations with P_{acc_3d} in similar

469   regions (Fig. 10b). For non-rainy days, vapor $\delta^{18}O$ and d-excess still show significant correlations with P_{acc_3d} at

470   regional scale, albeit with weaker correlation levels and smaller spatial extent (Fig. S11). These significant

471   correlations among vapor $\delta^{18}O$, d-excess, and P_{acc_3d} provide further evidence for understanding processes that are

472   responsible for the amount effect. The negative correlation between $\delta^{18}O$ and P_{acc_3d} has also been observed in

473   precipitation and can be interpreted in terms of either continuous rainout (Cai and Tian, 2016; Scholl et al., 2009;

474   Vuille et al., 2003) or the effect of rain-vapor interaction (Lawrence et al., 2004; Risi et al., 2008a; Kurita et al.,

475   2011; Worden et al., 2007). Although continuous rainout with increased rainfall amount can explain the decreasing

476   trend of $\delta^{18}O$ by the Rayleigh distillation model, d-excess stays at a relatively stable level when specific humidity

477   is not very low (above ~4 g kg^{-1} in Fig. 3b for example). Therefore, the positive correlation between vapor d-excess

478   and P_{acc_3d} provides an additional constraint that the amount effect is not simply a result of rainout but rain-vapor

479   interaction plays an important role in altering lower tropospheric isotope compositions.
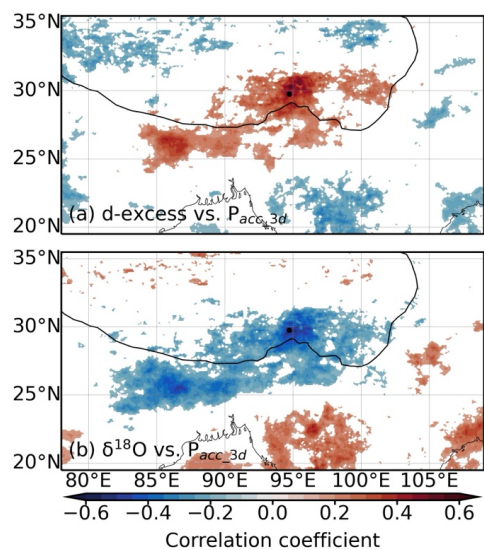
Figure 10. Relationships between vapor isotope compositions for rainy days (local daily precipitation amount not less than 2 mm) and total precipitation amount at the regional scale during the summer monsoon season. (a) spatial distribution of correlation coefficients between vapor d-excess and total precipitation amount during 3 days prior sampling (P_{acc_3d}). (b) is the same as (a) but for $\delta^{18}O$. Only values significant at the 95% significance level are shown. The black dots indicate the location of the SETP station. The black solid lines denote the Tibetan Plateau with altitude contour at 3000 m.

4.4 An alternative interpretation for the high d-excess in high-altitude TP ice cores

Interpretations of d-excess in meteoric water and ice cores on the TP are complicated by evaporation conditions over the northern Indian Ocean (RH_{SST} and SST) and continental recycling (Shao et al., 2021; Zhao et al., 2012; Joswiak et al., 2013; Pang et al., 2012; An et al., 2017). Attempts have been made to establish a relationship between vapor d-excess and RH_{STT} (Chen et al., 2024; Liu et al., 2024) as well as between ice core d-excess and RH_{STT} (Shao et al., 2021) or SST (Zhao et al., 2012). Based on relationships between vapor d-excess and surface evaporation conditions discussed above, however, the apparent relationships are mainly a result of similarities in the seasonality

494   of these variables. Furthermore, the direct contribution of water vapor contained in air masses over oceanic regions

495   to humidity at SETP is very limited (Fig. 4), which implies that the contribution to humidity over the TP is further

496   decreased than at SETP as it is at the forefront of moisture transport toward TP (Fig. S1). The dominant terrestrial

497   origin indicates that the moisture has undergone a certain degree of continental recycling. Mixing with terrestrial

498   sources is also reflected in the relationship between isotope compositions and q (Fig. 3). The degree of continental

499   recycling also alters vapor isotope compositions that transpiration introduces isotopically enriched moisture and

500   evaporation introduces moisture with high d-excess. Seasonally changing isotope signatures in precipitation and ice

501   cores as well as variations at longer timescales have been interpreted as moisture source shift between recycled

502   moisture over terrestrial regions and oceanic moisture sources or their relative contributions (An et al., 2017; Yang

503   and Yao, 2020). A further inference of this process is that the oceanic moisture is brought by the summer monsoon

504   while the westerlies bring moisture from continental recycling or even the Mediterranean Sea, and therefore water

505   isotope signatures reflect the interplay between the summer monsoon and westerlies (Joswiak et al., 2013; Pang et

506   al., 2012; Tian et al., 2007). Although our results also indicate seasonally shifting moisture sources, continental

507   recycling prevails throughout the year (Fig. 4). Besides focusing on moisture sources at the Earth surface, we

508   provide an alternative perspective to explain the high d-excess induced by the westerlies as dry and cold air

509   intrusions. In this circumstance, the interpretation of the interplay between the summer monsoon and westerlies is

510   still valid, but we emphasize changes in air mass property driven by the different circulation systems.

511   The proposed alternative interpretation could also help understand the increasing trend of precipitation and

512   river water isotope observations toward ice cores at higher altitudes on the TP as specific humidity is very low at

513   ice core sites and prolonged interaction with cold and dry air may further modify snow isotope compositions (Ma

514   et al., 2024; Wahl et al., 2022). In addition, intense rain-vapor interaction during the summer monsoon is another

515   source of higher vapor d-excess (section 4.3). Higher vapor d-excess signal could be inherited in subsequent

516 precipitation when it feeds the precipitation (Risi et al., 2008b). However, a clear relationship between TP

517 precipitation *d*-excess and monsoon convection has not been established yet, partly due to less attention has been

518 paid to *d*-excess in previous studies. Nevertheless, summer monsoon rainfall *d*-excess observed on the TP is

519 generally between 0-10‰ (Tian et al., 2001). Raindrop evaporation at upstream increases vapor *d*-excess and

520 therefore could cause elevated *d*-excess in downstream rainfall. On the contrary, this effect can be compensated by

521 on-site raindrop evaporation as it lowers raindrop *d*-excess values. The overall positive correlation between

522 precipitation *d*-excess and altitude in Asia has been sometimes interpreted as stronger evaporation at lower altitudes

523 (Bershaw, 2018). For snowfall on glaciers, evaporation is less likely for falling snowflakes due to cold temperatures

524 and the short distance between the cloud base and the glacier surface. Therefore, elevated vapor *d*-excess signal

525 caused by accumulated rain-vapor interaction at upstream associated with monsoon convection could be another

526 source for the high *d*-excess in ice cores.

527 **5 Conclusions**

528 We present a three-year-long daily near-surface water vapor isotope compositions observed at the South-East

529 TP station which is at the major channel for moisture entering the TP. Our vapor isotope compositions paired with

530 specific humidity reflect distinct moisture sources and dynamics between the non-monsoon and summer monsoon

531 seasons, consistent with Lagrangian moisture diagnostic results. Despite significant negative correlations between

532 vapor *d*-excess and relative humidity scaled to sea surface temperature existing over the northern Indian Ocean

533 when data for all seasons are considered, such correlations with oceanic surface evaporation conditions largely

534 disappear when separately considering each season. This result questions the early interpretation of TP *d*-excess as

535 oceanic evaporation conditions and guarantees new interpretations in the future.

536 During the non-monsoon season, vapor *d*-excess is mainly influenced by specific humidity both at the local

537   scale and upstream. Highly dehydrated air at the lower end of the Rayleigh distillation is expected to have extremely

538   high d-excess values. Air mass trajectory analyses and moisture source diagnostics suggest that the cold and dry air

539   intrusion driven by the westerlies during the non-monsoon season leads to the increasing trend of vapor d-excess

540   along with decreasing specific humidity. This process also contributes to a weak negative correlation between vapor

541   d-excess and $\delta^{18}O$. Furthermore, vapor $\delta^{18}O$ primarily reflects mixing processes with a relatively enriched moist

542   end-member compared with the summer monsoon season. The new insight on non-monsoon season vapor d-excess

543   provides an alternative way to interpret the high d-excess in high-altitude TP ice cores.

544   During the summer monsoon season, rain evaporation is the dominant process determining water vapor isotope

545   compositions. First, vapor $\delta^{18}O$ systematically shifts below the Rayleigh distillation curve falling in the region

546   predicted by "super-Rayleigh" distillation driven by partial rain evaporation. Second, vapor $\delta^{18}O$ is anti-correlated

547   with d-excess pointing to an origin of depleted vapor by kinetic fractionation which is not likely simply a result of

548   rainout. Third, vapor $\delta^{18}O$ is significantly negatively correlated with total precipitation amount at the regional scale,

549   but vapor d-excess positively correlates with total precipitation amount. These results help us understand the

550   dynamics of atmospheric humidity and also help disentangle the different effects of rainout and rain-vapor

551   interaction in the amount effect.

552   Overall, the new findings from the study reveal different moisture sources and dynamics between the non-

553   monsoon and monsoon seasons over the southeastern TP. The findings will also help the interpretation of ice core

554    $\delta^{18}O$ and d-excess records derived from glaciers on the TP.

555   **Competing interests**

556   The authors declare that they have no conflict of interest.

557 **Acknowledgements**

558   This research is supported by the National Natural Science Foundation of China (Grant 42371144), the Yunnan

559 Fundamental Research Projects (Grant 202301AT070183), and the funding of Donglu Talent Young Scholar from

560 the Yunnan University and support for young scholars from the Double First-Class Initiative for Ecological

561 Disciplines of the Yunnan University. We would like to thank the staff at the South-East Tibetan Plateau Station for

562 integrated observation and research of alpine environment for their help in collecting water samples and for sharing

563 the meteorological data at the station.

564 **Data availability**

565   The NOAA ARL provided the HYSPLIT model and the GDAS data

566 (https://www.ready.noaa.gov/HYSPLIT.php). The Copernicus Climate Change Service provided the ERA5 data

567 (https://doi.org/10.24381/cds.adbb2d47 and https://doi.org/10.24381/cds.f17050d7). The GPM data are available

568 through GES DISC (https://doi.org/10.5067/GPM/IMERG/3B-HH/07). Local meteorological data at the SETP

569 station are provided by National Tibetan Plateau / Third Pole Environment Data Center

570 (https://dx.doi.org/10.11888/AtmosphericPhysics.tpe.68.db). The observation data at the SETP station have been

571 uploaded to Figshare and will be made publicly available after publication (10.6084/m9.figshare.27302871).

572 **Author contributions**

573   **Zhongyin Cai**: Conceptualization, methodology, investigation, formal analysis, funding acquisition, writing-

574 original draft, writing-review & editing; **Rong Li**: Investigation, data curation, writing-review & editing; **Cheng**

575 **Wang**: Validation; **Qiukai Mao**: Investigation, **Lide Tian**: Resources, project administration, funding acquisition.

References

Aemisegger, F., Pfahl, S., Sodemann, H., Lehner, I., Seneviratne, S. I., and Wernli, H.: Deuterium excess as a proxy for continental moisture recycling and plant transpiration, Atmos. Chem. Phys., 14, 4029-4054, 10.5194/acp-14-4029-2014, 2014.

An, W., Hou, S., Zhang, Q., Zhang, W., Wu, S., Xu, H., Pang, H., Wang, Y., and Liu, Y.: Enhanced Recent Local Moisture Recycling on the Northwestern Tibetan Plateau Deduced From Ice Core Deuterium Excess Records, J. Geophys. Res., 122, 12,541-512,556, 10.1002/2017jd027235, 2017.

Araguás-Araguás, L., Fröehlich, K., and Rozanski, K.: Stable isotope composition of precipitation over southeast Asia, J. Geophys. Res., 103, 28721-28742, 1998.

Benetti, M., Reverdin, G., Pierre, C., Merlivat, L., Risi, C., Steen-Larsen, H. C., and Vimeux, F.: Deuterium excess in marine water vapor: Dependency on relative humidity and surface wind speed during evaporation, J. Geophys. Res., 119, 584-593, 2014.

Bershaw, J.: Controls on Deuterium Excess across Asia, Geosciences, 8, 257, 10.3390/geosciences8070257, 2018.

Bonne, J.-L., Behrens, M., Meyer, H., Kipfstuhl, S., Rabe, B., Schönicke, L., Steen-Larsen, H. C., and Werner, M.: Resolving the controls of water vapour isotopes in the Atlantic sector, Nature Communications, 10, 1632, 10.1038/s41467-019-09242-6, 2019.

Bonne, J. L., Masson-Delmotte, V., Cattani, O., Delmotte, M., Risi, C., Sodemann, H., and Steen-Larsen, H. C.: The isotopic composition of water vapour and precipitation in Ivittuut, southern Greenland, Atmos. Chem. Phys., 14, 4419-4439, 10.5194/acp-14-4419-2014, 2014.

Bony, S., Risi, C., and Vimeux, F.: Influence of convective processes on the isotopic composition (δ^{18}O and δD) of precipitation and water vapor in the tropics: 1. Radiative-convective equilibrium and Tropical Ocean–Global Atmosphere–Coupled Ocean-Atmosphere Response Experiment (TOGA-COARE) simulations, J. Geophys. Res., 113, D19305, 10.1029/2008JD009942, 2008.

Bowen, G. J. and Wilkinson, B.: Spatial distribution of δ^{18}O in meteoric precipitation, Geology, 30, 315, 10.1130/0091-7613(2002)030<0315:sdooim>2.0.co;2, 2002.

Bowen, G. J., Cai, Z., Fiorella, R. P., and Putman, A.: Isotopes in the Water Cycle: Regional- to Global-Scale Patterns and Applications, Annu. Rev. Earth Planet. Sci., 47, 453-479, 10.1146/annurev-earth-053018-060220, 2019.

Breitenbach, S. F. M., Adkins, J. F., Meyer, H., Marwan, N., Kumar, K. K., and Haug, G. H.: Strong influence of water vapor source dynamics on stable isotopes in precipitation observed in Southern Meghalaya, NE India, Earth Planet. Sci. Lett., 292, 212-220, 10.1016/j.epsl.2010.01.038, 2010.

Cai, Z. and Tian, L.: Atmospheric controls on seasonal and interannual variations in the precipitation isotope in the East Asian Monsoon region, J. Climate, 29, 1339-1352, 10.1175/JCLI-D-15-0363.1, 2016.

Cai, Z. and Tian, L.: What causes the post-monsoon ^{18}O depletion over Bay of Bengal head and beyond?, Geophys. Res. Lett., 47, e2020GL086985, 10.1029/2020gl086985, 2020.

Cai, Z., Tian, L., and Bowen, G. J.: ENSO variability reflected in precipitation oxygen isotopes across the Asian Summer Monsoon region, Earth Planet. Sci. Lett., 475, 25-33, 10.1016/j.epsl.2017.06.035, 2017.

Cai, Z., Tian, L., and Bowen, G. J.: Spatial-seasonal patterns reveal large-scale atmospheric controls on Asian Monsoon precipitation water isotope ratios, Earth Planet. Sci. Lett., 503, 158-169, 10.1016/j.epsl.2018.09.028, 2018.

Cao, R., Huang, H., Wu, G., Han, D., Jiang, Z., Di, K., and Hu, Z.: Spatiotemporal variations in the ratio of transpiration to evapotranspiration and its controlling factors across terrestrial biomes, Agr. Forest Meteorol., 321, 108984, 10.1016/j.agrformet.2022.108984, 2022.

618   Chen, M., Gao, J., Luo, L., Zhao, A., Niu, X., Yu, W., Liu, Y., and Chen, G.: Temporal variations of stable isotopic
619   compositions in atmospheric water vapor on the Southeastern Tibetan Plateau and their controlling factors, Atmos. Res.,
620   303, 10.1016/j.atmosres.2024.107328, 2024.

621   Craig, H.: Isotopic Variations in Meteoric Waters, Science, 133, 1702-1703, 10.1126/science.133.3465.1702, 1961.

622   Craig, H. and Gordon, L. I.: Deuterium and oxygen 18 variations in the ocean and the marine atmosphere, in: Stable
623   Isotopes in Oceanographic Studies and Paleotemperatures. Spoleto, Tongiorgi, E., Italy, 9-130, 1965.

624   Dai, D., Gao, J., Steen-Larsen, H. C., Yao, T., Ma, Y., Zhu, M., and Li, S.: Continuous monitoring of the isotopic
625   composition of surface water vapor at Lhasa, southern Tibetan Plateau, Atmos. Res., 264,
626   10.1016/j.atmosres.2021.105827, 2021.

627   Dansgaard, W.: Stable isotopes in precipitation, Tellus, 16, 436-468, 10.1111/j.2153-3490.1964.tb00181.x, 1964.

628   Dütsch, M., Pfahl, S., and Sodemann, H.: The impact of nonequilibrium and equilibrium fractionation on two
629   different deuterium excess definitions, J. Geophys. Res., 122, 12732-12746, 10.1002/2017JD027085, 2017.

630   Fiorella, R. P., Poulsen, C. J., and Matheny, A. M.: Seasonal Patterns of Water Cycling in a Deep, Continental
631   Mountain Valley Inferred from Stable Water Vapor Isotopes, J. Geophys. Res., 123, 7271-7291,
632   doi:10.1029/2017JD028093, 2018.

633   Galewsky, J., Steen-Larsen, H. C., Field, R. D., Worden, J., Risi, C., and Schneider, M.: Stable isotopes in
634   atmospheric water vapor and applications to the hydrologic cycle, Rev. Geophys., 54, 809-865, 10.1002/2015RG000512,
635   2016.

636   Good, S. P., Noone, D., and Bowen, G.: Hydrologic connectivity constrains partitioning of global terrestrial water
637   fluxes, Science, 349, 175-177, 10.1126/science.aaa5931, 2015.

638   Guo, R., Yu, W., Zhang, J., Lewis, S., Lazhu, Ma, Y., Xu, B., Wu, G., Jing, Z., Ren, P., Zhang, Z., Wang, Q., and Qu,
639   D.: Different Dynamics Drive Indian Ocean Moisture to the Southern Slope of Central Himalayas: An Isotopic Approach,
640   Geophys. Res. Lett., 51, 10.1029/2024gl109359, 2024.

641   Han, J., Tian, L., Cai, Z., Ren, W., Liu, W., Li, J., and Tai, J.: Season-specific evapotranspiration partitioning using
642   dual water isotopes in a Pinus yunnanensis ecosystem, southwest China, J. Hydrol., 608, 127672,
643   10.1016/j.jhydrol.2022.127672, 2022.

644   He, Y., Risi, C., Gao, J., Masson-Delmotte, V., Yao, T., Lai, C.-T., Ding, Y., Worden, J., Frankenberg, C., Chepfer,
645   H., and Cesana, G.: Impact of atmospheric convection on south Tibet summer precipitation isotopologue composition
646   using a combination of in situ measurements, satellite data and atmospheric general circulation modeling, J. Geophys.
647   Res., 120, 3852-3871, 10.1002/2014JD022180, 2015.

648   Hersbach, H., Bell, W., Berrisford, P., Horányi, A., J., M.-S., Nicolas, J., Radu, R., Schepers, D., Simmons, A., Soci,
649   C., and Dee, D.: Global reanalysis: goodbye ERA-Interim, hello ERA5, 10.21957/vf291hehd7,   2019.

650   Huffman, G. J., Stocker, E. F., Bolvin, D. T., Nelkin, E. J., and Tan, J.: GPM IMERG Final Precipitation L3 Half
651   Hourly 0.1 degree x 0.1 degree V07, Greenbelt, MD, Goddard Earth Sciences Data and Information Services Center (GES
652   DISC) [dataset], 10.5067/GPM/IMERG/3B-HH/07, 2023.

653   Jiang, J., Zhou, T., Qian, Y., Li, C., Song, F., Li, H., Chen, X., Zhang, W., and Chen, Z.: Precipitation regime changes
654   in High Mountain Asia driven by cleaner air, Nature, 10.1038/s41586-023-06619-y, 2023.

655   Joswiak, D. R., Yao, T., Wu, G., Tian, L., and Xu, B.: Ice-core evidence of westerly and monsoon moisture
656   contributions in the central Tibetan Plateau, J. Glaciol., 59, 56-66, 10.3189/2013JoG12J035, 2013.

657   Keeling, C. D.: The concentration and isotopic abundances of atmospheric carbon dioxide in rural areas, Geochim.
658   Cosmochim. Acta, 13, 322-334, 10.1016/0016-7037(58)90033-4, 1958.

659   Kurita, N., Noone, D., Risi, C., Schmidt, G. A., Yamada, H., and Yoneyama, K.: Intraseasonal isotopic variation
660   associated with the Madden-Julian Oscillation, J. Geophys. Res., 116, D24101, 10.1029/2010JD015209, 2011.

661   Lawrence, J. R., Gedzelman, S. D., Dexheimer, D., Cho, H.-K., Carrie, G. D., Gasparini, R., Anderson, C. R.,

662   Bowman, K. P., and Biggerstaff, M. I.: Stable isotopic composition of water vapor in the tropics, J. Geophys. Res., 109,
663   D06115, 10.1029/2003JD004046, 2004.

664   Lee, J.-E. and Fung, I.: "Amount effect" of water isotopes and quantitative analysis of post-condensation processes,
665   Hydrol. Processes, 22, 1-8, 10.1002/hyp.6637, 2008.

666   Lekshmy, P. R., Midhun, M., and Ramesh, R.: Role of moisture transport from Western Pacific region on water vapor
667   isotopes over the Bay of Bengal, Atmos. Res., 265, 10.1016/j.atmosres.2021.105895, 2022.

668   Liu, F., Tian, L., Cai, Z., Wang, X., Liang, P., Wang, S., and Li, S.: What caused the lag between oxygen-18 and
669   deuterium excess in atmospheric vapor and precipitation during the earlier summer season in southwest China?, J. Hydrol.,
670   644, 10.1016/j.jhydrol.2024.132087, 2024.

671   Liu, J., Xiao, C., Ding, M., and Ren, J.: Variations in stable hydrogen and oxygen isotopes in atmospheric water
672   vapor in the marine boundary layer across a wide latitude range, Journal of Environmental Sciences, 26, 2266-2276,
673   10.1016/j.jes.2014.09.007, 2014.

674   Luo, L.: Meteorological observation data from the integrated observation and research station of the alpine
675   environment in Southeast Tibet (2007-2017), National Tibetan Plateau Data Center [dataset],
676   10.11888/AtmosphericPhysics.tpe.68.db, 2018.

677   Ma, T., Jiang, Z., Ding, M., He, P., Li, Y., Zhang, W., and Geng, L.: A model framework for atmosphere–snow water
678   vapor exchange and the associated isotope effects at Dome Argus, Antarctica – Part 1: The diurnal changes, The
679   Cryosphere, 18, 4547-4565, 10.5194/tc-18-4547-2024, 2024.

680   Merlivat, L. and Jouzel, J.: Global climatic interpretation of the deuterium-oxygen 18 relationship for precipitation,
681   J. Geophys. Res., 84, 5029-5033, 1979.

682   Noone, D.: Pairing Measurements of the Water Vapor Isotope Ratio with Humidity to Deduce Atmospheric
683   Moistening and Dehydration in the Tropical Midtroposphere, J. Climate, 25, 4476-4494, 10.1175/jcli-d-11-00582.1, 2012.

684   Pang, H., Hou, S., Kaspari, S., Mayewski, P., Introne, D., Masson-Delmotte, V., Jouzel, J., Li, Z., He, Y., Hong, S.,
685   and Qin, D.: Atmospheric circulation change in the central Himalayas indicated by a high-resolution ice core deuterium
686   excess record, Climate Research, 53, 1-12, 10.3354/cr01090, 2012.

687   Putman, A. L., Fiorella, R. P., Bowen, G. J., and Cai, Z.: A Global Perspective on Local Meteoric Water Lines: Meta-
688   analytic Insight into Fundamental Controls and Practical Constraints, Water Resour. Res., 55, 6896-6910,
689   10.1029/2019wr025181, 2019.

690   Risi, C., Bony, S., and Vimeux, F.: Influence of convective processes on the isotopic composition (δ^{18}O and δD) of
691   precipitation and water vapor in the tropics: 2. Physical interpretation of the amount effect, J. Geophys. Res., 113, D19306,
692   10.1029/2008JD009943, 2008a.

693   Risi, C., Bony, S., Vimeux, F., Descroix, L., Ibrahim, B., Lebreton, E., Mamadou, I., and Sultan, B.: What controls
694   the isotopic composition of the African monsoon precipitation? Insights from event-based precipitation collected during
695   the 2006 AMMA field campaign, Geophys. Res. Lett., 35, L24808, 10.1029/2008GL035920, 2008b.

696   Samuels-Crow, K. E., Galewsky, J., Sharp, Z. D., and Dennis, K. J.: Deuterium excess in subtropical free troposphere
697   water vapor: Continuous measurements from the Chajnantor Plateau, northern Chile, Geophys. Res. Lett., 41, 8652-8659,
698   10.1002/2014gl062302, 2014.

699   Sayres, D. S., Pfister, L., Hanisco, T. F., Moyer, E. J., Smith, J. B., St. Clair, J. M., O'Brien, A. S., Witinski, M. F.,
700   Legg, M., and Anderson, J. G.: Influence of convection on the water isotopic composition of the tropical tropopause layer
701   and tropical stratosphere, J. Geophys. Res., 115, 10.1029/2009JD013100, 2010.

702   Scholl, M. A., Shanley, J. B., Zegarra, J. P., and Coplen, T. B.: The stable isotope amount effect: New insights from
703   NEXRAD echo tops, Luquillo Mountains, Puerto Rico, Water Resour. Res., 45, 10.1029/2008wr007515, 2009.

704   Shao, L., Tian, L., Cai, Z., Wang, C., and Li, Y.: Large-scale atmospheric circulation influences the ice core d-excess
705   record from the central Tibetan Plateau, Clim. Dyn., 57, 1805-1816, 10.1007/s00382-021-05779-9, 2021.

Sodemann, H., Schwierz, C., and Wernli, H.: Interannual variability of Greenland winter precipitation sources: Lagrangian moisture diagnostic and North Atlantic Oscillation influence, J. Geophys. Res., 113, 10.1029/2007jd008503, 2008.

Sodemann, H., Aemisegger, F., Pfahl, S., Bitter, M., Corsmeier, U., Feuerle, T., Graf, P., Hankers, R., Hsiao, G., Schulz, H., Wieser, A., and Wernli, H.: The stable isotopic composition of water vapour above Corsica during the HyMeX SOP1 campaign: insight into vertical mixing processes from lower-tropospheric survey flights, Atmos. Chem. Phys., 17, 6125-6151, 10.5194/acp-17-6125-2017, 2017.

Steen-Larsen, H. C., Risi, C., Werner, M., Yoshimura, K., and Masson-Delmotte, V.: Evaluating the skills of isotope-enabled General Circulation Models against in-situ atmospheric water vapor isotope observations, J. Geophys. Res., 122, 246-263, 10.1002/2016JD025443, 2017.

Stein, A. F., Draxler, R. R., Rolph, G. D., Stunder, B. J. B., Cohen, M. D., and Ngan, F.: NOAA's HYSPLIT atmospheric transport and dispersion modeling system, Bull. Am. Meteorol. Soc., 96, 2059-2077, 10.1175/BAMS-D-14-00110.1, 2015.

Terzer-Wassmuth, S., Wassenaar, L. I., Welker, J. M., and Araguas-Araguas, L. J.: Improved High-Resolution Global and Regionalized Isoscapes of δ18O, δ2H, and d-Excess in Precipitation, Hydrol. Processes, 35, 10.1002/hyp.14254, 2021.

Thompson, L. G., Yao, T., E.Mosley-Thompson, Davis, M. E., Henderson, K. A., and Lin, P.-N.: A High-Resolution Millennial Record of the South Asian Monsoon from Himalayan Ice Cores, Science, 289, 1916-1919, 10.1126/science.289.5486.1916, 2000.

Thompson, L. G., Yao, T. D., Davis, M. E., Mosley-Thompson, E., Synal, H. A., Wu, G., Bolzan, J. F., Kutuzov, S., Beaudon, E., Sierra-Hernández, M. R., and Beer, J.: Ice core evidence for an orbital-scale climate transition on the Northwest Tibetan Plateau, Quat. Sci. Rev., 324, 10.1016/j.quascirev.2023.108443, 2024.

Tian, L., Masson-Delmotte, V., Stievenard, M., Yao, T., and Jouzel, J.: Tibetan Plateau summer monsoon northward extent revealed by measurements of water stable isotopes, J. Geophys. Res., 106, 28081-28088, 10.1029/2001JD900186, 2001.

Tian, L., Yao, T., MacClune, K., White, J. W. C., Schilla, A., Vaughn, B., Vachon, R., and Ichiyanagi, K.: Stable isotopic variations in west China: A consideration of moisture sources, J. Geophys. Res., 112, D10112, 10.1029/2006jd007718, 2007.

Tian, L., Yu, W., Schuster, P. F., Wen, R., Cai, Z., Wang, D., Shao, L., Cui, J., and Guo, X.: Control of seasonal water vapor isotope variations at Lhasa, southern Tibetan Plateau, J. Hydrol., 580, 124237, 10.1016/j.jhydrol.2019.124237, 2020.

Uemura, R., Matsui, Y., Yoshimura, K., Motoyama, H., and Yoshida, N.: Evidence of deuterium excess in water vapor as an indicator of ocean surface conditions, J. Geophys. Res., 113, 10.1029/2008jd010209, 2008.

Vuille, M., Bradley, R. S., Werner, M., Healy, R., and Keimig, F.: Modeling δ18O in precipitation over the tropical Americas: 1. Interannual variability and climatic controls, J. Geophys. Res., 108, 4174, 10.1029/2001JD002038, 2003.

Wahl, S., Steen-Larsen, H. C., Hughes, A. G., Dietrich, L. J., Zuhr, A., Behrens, M., Faber, A.-K., and Hörhold, M.: Atmosphere-Snow Exchange Explains Surface Snow Isotope Variability, Geophys. Res. Lett., 49, e2022GL099529, 10.1029/2022GL099529, 2022.

Webster, C. R. and Heymsfield, A. J.: Water isotope ratios D/H, 18O/16O, 17O/16O in and out of clouds map dehydration pathways, Science, 302, 1742-1745, 10.1126/science.1089496, 2003.

Wei, Z. and Lee, X.: The utility of near-surface water vapor deuterium excess as an indicator of atmospheric moisture source, J. Hydrol., 123923, 10.1016/j.jhydrol.2019.123923, 2019.

Welp, L. R., Lee, X., Griffis, T. J., Wen, X. F., Xiao, W., Li, S., Sun, X., Hu, Z., Val Martin, M., and Huang, J.: A meta-analysis of water vapor deuterium-excess in the midlatitude atmospheric surface layer, Global Biogeochem. Cycles, 26, 10.1029/2011gb004246, 2012.

Worden, J., Noone, D., and Bowman, K.: Importance of rain evaporation and continental convection in the tropical water cycle, Nature, 445, 528-532, 10.1038/nature05508, 2007.

Wu, F., Fang, X., Yang, Y., Dupont-Nivet, G., Nie, J., Fluteau, F., Zhang, T., and Han, W.: Reorganization of Asian climate in relation to Tibetan Plateau uplift, Nature Reviews Earth & Environment, 10.1038/s43017-022-00331-7, 2022.

Yang, X. and Yao, T.: Seasonality of moisture supplies to precipitation over the Third Pole: a stable water isotopic perspective, Sci Rep, 10, 15020, 10.1038/s41598-020-71949-0, 2020.

Yang, X., Davis, M. E., Acharya, S., and Yao, T.: Asian monsoon variations revealed from stable isotopes in precipitation, Clim. Dyn., 51, 2267-2283, 10.1007/s00382-017-4011-4, 2017.

Yao, T., Masson-Delmotte, V., Gao, J., Yu, W., Yang, X., Risi, C., Sturm, C., Werner, M., Zhao, H., He, Y., Ren, W., Tian, L., Shi, C., and Hou, S.: A review of climatic controls on δ^{18}O in precipitation over the Tibetan Plateau: Observations and simulations, Rev. Geophys., 51, 525-548, 10.1002/rog.20023, 2013.

Yao, T., Bolch, T., Chen, D., Gao, J., Immerzeel, W., Piao, S., Su, F., Thompson, L., Wada, Y., Wang, L., Wang, T., Wu, G., Xu, B., Yang, W., Zhang, G., and Zhao, P.: The imbalance of the Asian water tower, Nature Reviews Earth & Environment, 3, 618-632, 10.1038/s43017-022-00299-4, 2022.

Yu, W., Tian, L., Ma, Y., Xu, B., and Qu, D.: Simultaneous monitoring of stable oxygen isotope composition in water vapour and precipitation over the central Tibetan Plateau, Atmos. Chem. Phys., 15, 10251-10262, 10.5194/acp-15-10251-2015, 2015.

Yu, W., Tian, L., Risi, C., Yao, T., Ma, Y., Zhao, H., Zhu, H., He, Y., Xu, B., Zhang, H., and Qu, D.: δ^{18}O records in water vapor and an ice core from the eastern Pamir Plateau: Implications for paleoclimate reconstructions, Earth Planet. Sci. Lett., 456, 146-156, 10.1016/j.epsl.2016.10.001, 2016.

Zhang, Q., Shen, Z., Pokhrel, Y., Farinotti, D., Singh, V. P., Xu, C.-Y., Wu, W., and Wang, G.: Oceanic climate changes threaten the sustainability of Asia's water tower, Nature, 615, 87-93, 10.1038/s41586-022-05643-8, 2023.

Zhao, H., Xu, B., Li, Z., Wang, M., Li, J., and Zhang, X.: Abundant climatic information in water stable isotope record from a maritime glacier on southeastern Tibetan Plateau, Clim. Dyn., 48, 1161-1171, 10.1007/s00382-016-3133-4, 2017.

Zhao, H., Xu, B., Yao, T., Wu, G., Lin, S., Gao, J., and Wang, M.: Deuterium excess record in a southern Tibetan ice core and its potential climatic implications, Clim. Dyn., 38, 1791-1803, 10.1007/s00382-011-1161-7, 2012.